Geometry of vegetation patterns: understanding patterns in dryland ecosystems and beyond

Jaïbi, O.

1

Introduction

Understanding nature has been one of mankind's biggest yearnings. We are continuously trying to decipher nature's adjustments as a complex environment of which we, the human species, only represents a fraction, albeit a very impactful one [50]. A universal feature of nature is its ability to adapt to external shifting factors. This adaptation results in catastrophic changes [130, 131, 160]- such as the extinction of animal species [17] - or gradual ones, evolving towards, conceivably temporary, new states [81].

One of the major shifting factors throughout history has been climate change, especially since the Industrial Revolution [110]. Climate change is, arguably, the most severe challenge facing planet Earth during the 21st century [57], also according to the United Nations [3].

Soil degradation - which is mainly caused by human activities - has a direct impact on climate change [149, 156]. This directly results in desertification, a form of land degradation in arid and semi-arid areas. Arid and semi-arid areas are land surfaces receiving less than $400mm$ of annual precipitation [167]. They cover more than 40% of the global land surface [37]. This development has led to escalating concerns about the impact of climate change on desertification and biodiversity loss [5, 47], thereby propelling the search for indicators of imminent ecosystem shifts and the understanding thereof – from a theoretical perspective – in the last two decades. In addition to that, aerial photographs and, later on, satellite images have opened up a research field area that goes beyond laboratory dimensions, trying to understand the mysteries of these landscapes such as spatial plant distributions [58, 78, 102, 112, 152].

One emergent feature that came to light while studying (semi-)arid landscapes with the aid of aerial photographs, is nature's adaptability to 'self-organize' in order to sustain itself under changing environmental conditions [32, 102, 106].

Self-organization is the emergence of patterns and order in a system by internal processes, rather than external constraints or forces [68]. As a result, local interactions between individuals may often spawn global features. Self-organization and the formation of patterns encapsulates all fields and scales, from the smallest molecular DNA structure [85] to the Copernican solar system model [170] and beyond, making it a universal feature of nature. Ecological examples of self-organization range from the structure of animal social groups to spatial patterns associated with plant distributions [68]. A few visual examples are given in Figure 1.1.

(a) The cheetah has a spotted body with a stripy tail [4].

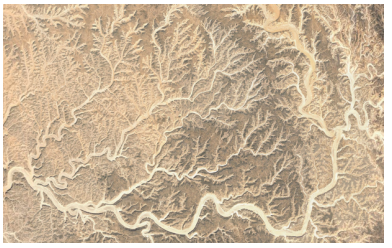

(b) Google Earth satellite image of a fractal pattern in the Egyptian desert (27°28′N; 32°14′E).

Figure 1.1: Different patterns at different scales in nature.

Vegetation patterns form a characteristic feature of semi-arid regions through the formation of distinct spatial plant distributions [137]. Water scarcity hampers the ecosystem into spatial separation of plants; patches of dense biomass and areas of bare soil appear, induced by a positive feedback between local vegetation growth and water redistribution towards areas of high biomass [126]. This manifests itself in different shapes and on different spatial scales as can be seen in Figure 1.2.

Lots of research within the ecological community has already been done about this specific type of land degradation [58, 61, 66, 87, 88, 100, 138, 141, 145, 161, 172, 176]. The proposed ecological models studied in these papers have already shown to numerically reproduce the vegetation patterns observed [14, 90, 124].

Given the magnitude and tragic consequences of the process of land degradation and desertification, a few questions naturally present themselves

- How does the study of vegetation patches in any way relate to mathematics where - stereotypically - research relies on pencil, paper and nowadays some computational power?

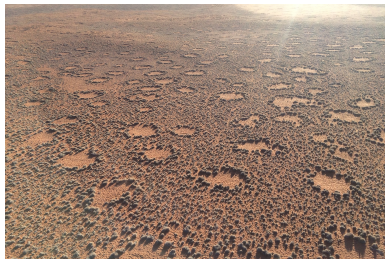

(a) Fairy circles in the Namibian desert [1].

(b) Striped pattern of woody vegetation (Acacia) that grows parallel to dry slopes in Australia [2].

Figure 1.2: Different vegetation patterns located in different parts of the world.

- How can the abstractness and clarity of mathematics help with the randomness and complexity of the real ecological world?
- Can ecology and mathematics fruitfully join efforts in order to get a better understanding and grasp of this pressing phenomenon?

The answers to these questions are not that simple nor straightforward. On the one hand, aerial observations do not form proof of a universal feature. Adding to that, solely relying on numerical simulations has it restrictions as the latter rely on a whole set of specific conditions, making it harder to formulate generalized statements about an ecosystem. On the other hand, the complexity of vegetation ecosystems limits rigorous mathematical analysis. Fortunately, pattern formation models can play an important role in validating (or refuting) the results acquired from topographical data and numerics.

The challenge and aim of this thesis is bridging the gap between ecology and mathematics, real world observations and theorems and finding a common ground to further build new research on. It transcends the study of spatial vegetation structures to enclose a whole variety of patterns that fit into the generalized mathematical framework of dynamical systems. The motivation behind this piece of work is threefold:

- To assess the extent to which conceptual models' predictions and results apply to real world observations as has been done in Chapter 2.
- To extend the ecological insights acquired from an ecosystem model and apply rigorous mathematical analysis to prove the existence of various (already observed) spatial patterns as has been done in Chapter 3.
- To exploit the rich nonlinear structure of an ecosystem model and to investigate the existence of a broad class of novel spatial patterns, both from an

ecological and a mathematical perspective as has been done in Chapter 3.

So how does mathematics lend a hand to ecology and vice versa? A few of the models proposed within the ecological community rely on reaction-(advection)-diffusion equations [14, 90, 124], which have played a key role in understanding the spatio-temporal evolution of complex dynamical systems. Two of these models are studied within this thesis, and have been meticulously selected to achieve the aims listed above: the most conceptual model at hand, in order to maximize data and model prediction comparison and in contrast, one of the most elaborated ecosystem models that had not been analyzed in such a mathematical way before. Both these models are, deducibly, or reaction-(advection)-diffusion type.

A reaction-diffusion equation, as the term suggests, comprises a reaction term and a diffusion term, describing the evolution in time and space of a certain concentration or density of a component of a system. The addition of a diffusion term to a reactive system, according to Turing [150], would disrupt a system in a way it may change from a homogeneous spatial state to a heterogeneous patterned state, giving rise to all sorts of spatial structures [150].

Pattern formation in this type of equations is of high interest both in ecology and mathematics. Understanding the cross-fertilization of ecology and mathematics along the specific problem at hand can be hard. The complexity of the domain of pattern formation compels the boundaries of different areas of research to fuse. Trying to bridge the gaps and breaches between different fields of science can be a tough quest, starting with the linguistic barrier of mere definitions and concepts. Therefore, a thorough and detailed presentation of the basics of each side of the spectrum is required, in order to set a firm and clear working ground to advance with.

First, an ecological background is given, exploring the methodologies and mechanisms preceding the models discussed. Second, an overview of the mathematical concepts and tools is given, as a basic foundation of the work within this thesis. Last but not least, a brief outline of the studies carried out in this work is presented.

1 Ecological background

The pattern of variation shown by the distribution of species among quadrants of the earth's surface chosen at random hovers in a tantalizing manner between the continuous and the discontinuous [164].

1.1 Ecological context

The complexity and diversity of factors involved in the study of ecological systems, in particular vegetation ecology, demands for a reflection on the scientific methodology adopted and for a diligent modeling approach. This has been cause for divisiveness within the ecological community since the early twentieth century [154]. However, the concept of patterns in vegetation had already become standard since Watt's 1947 paper on *pattern and process in the plant community* [163].

It is to be expected that the most consistent and clearest ecological patterns will almost invariably have several explanations, driven by various mechanisms all pulling in the same direction. According to Whittaker [166], two main principles are at play when it comes to spatial vegetation dynamics, forming the skeleton of the different modeling approaches adopted so far:

- The principle of species individuality – each species has its unique environmental requirements and distribution, according to its own genetic structure, physiological characteristics and population dynamics. The individualistic nature of the species reflects itself in the individualistic nature of plant community distributions.
- The principle of community continuity, i.e., continuum principle – communities which occur along continuous environmental gradients usually intergrade continuously, with gradual changes in population levels of species along the gradient.

These two principles resulted in two main modeling approaches in use in studies of plant population dynamics [106]; agent-based models, i.e., stochastic computational algorithms, based on the individuality principle and often capture the characteristics of a plant in great detail. The continuum principle was incorporated in partial differential equations (PDE's) which focus on deterministic processes at small spatial scales rather than addressing individual plants. The plant population is then described by a continuous biomass areal density [106]. The second approach has been adopted throughout this thesis, as it fits into the well-developed theory of PDE's. Within these ecosystem models, different types of environmental variables can be recognized, e.g. of abiotic or biotic type. Abiotic variables such as precipitation and soil nitrogen content directly determine plant growth and success. Biotic variables such as the competition from other plants, pathogens, herbivores and fungi (mycorrhizae), may be beneficial or detrimental to plant growth or have complex effects contingent on abiotic variables [154]. The main abiotic variable is the amount of water a plant can acquire in order to survive. Therefore, in order to understand the basic dynamics of plant population, most models have stripped these complex ecosystems to their "bare essentials": biomass and water, and the interaction thereof.

Water transport has two main effects; providing an extra source of water to vegetation patches as well as inhibiting vegetation growth in the patch surroundings. As shown and explained in Figure 1.3, there are different ways water transport contributes to biomass and root system growth.

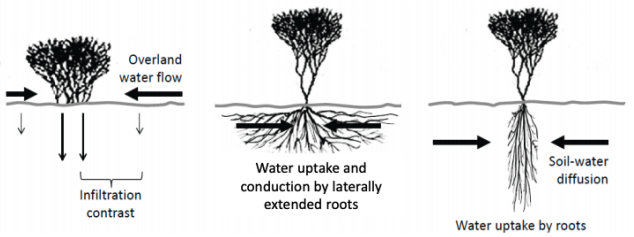

Figure 1.3: Schematic illustration of three different modes of water transport capable of inducing pattern-forming feedback in water-limited vegetation.
Left: Infiltration feedback: typically presents itself in soil areas covered in soil crust that change the rate of surface-water infiltration inducing overland-water flow towards densely vegetated areas.
Middle: Root-augmentation feedback: laterally extended root systems allow water uptake and conduction from a larger domain.
Right: Soil-water diffusion feedback: confined root systems create a soil-water gradient due to high water uptake resulting in lateral water diffusion [106].

The most simple reaction-(advection)-diffusion system of partial differential equation that would heuristically describe the dynamics of a plant population in a water-scarce environment takes the form

$$\begin{cases} \text{change in biomass} &= \text{growth - mortality + spread through seed dispersal,} \\ \text{change in water} &= \text{precipitation - evaporation - uptake + spread of water.} \end{cases} \tag{1.1}$$

In the above, the abiotic variable has been "limited" to precipitation and evaporation, i.e., water availability, and the biotic variable is modeled through seed dispersal and plant growth/mortality.

The above heuristic concept has been translated into several PDE models for dryland vegetation [62, 63, 90, 97, 124, 161]. The simplest two-component model that takes into account both biomass and water was proposed by Klausmeier [90]. The extended version of this model (system (1.2)) is studied in Chapter 2. More detailed models include two water variables representing soil-water content and overland-water flow [62, 79, 142].

Finding a fruitful balance in the realm of adequately modeling vegetation patterns in semi-arid ecosystems is a double-edged blade. Models that capture

the plant population dynamics in more detail are more advantageous in that they provide better defined and measurable parameters, though being less prone to mathematical analysis. In contrast, considering specific contexts for vegetation patterns such as steady rainfall, a single plant species, high soil-water diffusivity, allows for model simplifications that facilitate mathematical assessment of the model [107]. The latter method has been adopted for the analysis of the ecosystems studied, which we will present next.

1.2 Ecosystem models studied

> *"Dynamic models bridge over two other modeling concepts in ecology; descriptive models, which presents relationships between measured variables, either graphically or algebraically and conceptual models, which seek to unravel basic mechanisms that underlie observed behaviors, but remain at the level of qualitative propositions [106]."*

Two dynamical ecosystem models have been studied in detail in this thesis, both two-component reaction–diffusion models describing the interaction between plant biomass and water. They exhibit spatial vegetation patterns that have been observed in semi-arid regions [61, 102]. Both models have been analyzed from different perspectives and with different purposes. The mathematical processes and patterns enclosed within these two models are of the highest interest, from ecological and analytical perspectives. The proposed models do not only grant deeper understanding of the process of desertification but also dig into an even richer realm of patterns, with novel connections and mathematical frameworks that have yet to be explored in more detail.

The first model is the extended-Klausmeier model [155], based on the model proposed by Klausmeier [90]:

$$\begin{cases} \dfrac{\partial w}{\partial t} &= e\dfrac{\partial^2 w}{\partial x^2} + \dfrac{\partial (vw)}{\partial x} + a - w - wn^2, \\ \dfrac{\partial n}{\partial t} &= \dfrac{\partial^2 n}{\partial x^2} - mn + wn^2. \end{cases} \tag{1.2}$$

where $w(x,t) \geq 0$ and $n(x,t) \geq 0$ represent areal densities of soil water and biomass, respectively, and $x \in \mathbb{R}$, $t \in \mathbb{R}^+$ are the space and time coordinates. The reaction terms model the change in water as a combined effect of rainfall ($+a$), evaporation ($-w$) and uptake by plants ($-wn^2$). Note that the coupling to plants is nonlinear, as more plants enable a better uptake of water through a bigger root system. The change of plant biomass comes from mortality ($-mn$) and plant growth ($+wn^2$). Note here again that the plant growth scales nonlinearly, as

more present biomass encourages water uptake and thus growth. Dispersion by plants is modeled as diffusion and the movement of water as a combined effect of diffusion ($+e$) and advection. The latter is due to gradients in the terrain, which are proportional to the slope parameter v.

The second model is a reduced version of the three-component model proposed by Gilad et al. for flat terrains [63]:

$$\begin{cases} \dfrac{\partial \tilde{B}}{\partial T} &= \Lambda \tilde{W}\tilde{B}(1-\tilde{B}/K)(1+E\tilde{B}) - M\tilde{B} + D_B \dfrac{\partial^2 \tilde{B}}{\partial \tilde{X}^2}, \\ \dfrac{\partial \tilde{W}}{\partial T} &= P - N(1-R\tilde{B}/K)\tilde{W} - \Gamma \tilde{W}\tilde{B}(1+E\tilde{B}) + D_W \dfrac{\partial^2 \tilde{W}}{\partial \tilde{X}^2}, \end{cases} \tag{1.3}$$

where $\tilde{B}(\tilde{X},T) \geq 0$ and $\tilde{W}(\tilde{X},T) \geq 0$ represent areal densities of biomass and soil water, respectively, and $\tilde{X} \in \mathbb{R}$, $T \in \mathbb{R}^+$ are the space and time coordinates. In the biomass ($\tilde{B}$) equation, Λ represents the biomass growth rate coefficient, K the maximal standing biomass, E is a measure for the root-to-shoot ratio, M the plant mortality rate and D_B the seed-dispersal or clonal growth rate, while in the water ($\tilde{W}$) equation, P represents the precipitation rate, N the evaporation rate, R the reduction of the evaporation rate due to shading, Γ the water-uptake rate coefficient and D_W the effective soil water diffusivity. Notice that the power of the factor $(1 + E\tilde{B})$ in both equations is unity, whereas in the reduced model in [175] the power is two. This difference stems from the consideration in the study of one space dimension rather than two.

System (1.3) represents a similar set-up to system (1.2). The equation lacks a first derivative, that is, an advection term, as it is constrained to flat terrains. Note that the original three component model [62] does account for topography. A simple glimpse at both equations discloses that system (1.3) takes more parameters into account and exhibits a less trivial mathematical structure than system (1.2). This allows for a more realistic modeling of real ecosystems. In addition to reproducing banded vegetation, the model has also reproduced the famous fairy circles [14, 61].

A closer look at both models reveals more contrast. In the extended-Klausmeier model, plant growth is unbounded ($+wn^2$), while in the Gilad et al. model, it is bounded ($(1 - \tilde{B}/K)$). Once the biomass reaches a certain height, it "suffers" from self-shading, which prohibits the process of photosynthesis and therefore further growth. In addition, the water and biomass growth/loss in the extended-Klausmeier model are coupled nonlinearly in the same manner in both equations while in the Gilad et al. model, the coupling between the two variables is more elaborated.

From an ecological perspective, system (1.3), which represents the master equation of this thesis, thus accounts for a vaster parameter space and a more realistic representation of dryland ecosystems. Unfortunately, this also makes it harder to analyze and numerically simulate, as numerics require specific initial conditions, parameter values and boundary conditions. To be blunt, it boils down to trying to grasp the behavior of an infinite dimensional continuous space in a finite dimensional discrete manner, which has its obvious limitations. Rigorous mathematical analysis of ecosystems like (1.2) and (1.3) has formed a bridge between ecologists and mathematicians within the pattern formation community. Setting the basis for the methods used in this type of analysis naturally leads us to the mathematical part of this introduction.

1.3 Ecosystem dynamics

Consider the compactly reformulated PDE of system (1.3), as done in Appendix B of Chapter 3

$$\begin{cases} B_t &= (aW-1)\,B + WB^2 - WB^3 + B_{xx}, \\ W_t &= \Psi - \left[\Phi + \Omega B + \Theta B^2\right] W + \dfrac{1}{\varepsilon^2} W_{xx}, \end{cases} \tag{1.4}$$

where the emphasis has to be made on the introduction of the small parameter $\varepsilon^2 = \dfrac{D_B}{D_W} \ll 1$, that is, ε is asymptotically small compared to 1, which will play a crucial role in the tools presented in this introduction and in the proofs of Chapter 3.

The classical approach to studying systems like (1.4) is to search for stationary and/or uniformly traveling solutions, that is, solutions that are stationary with respect to a co-moving frame with constant speed c. Introduce a new coordinate $\xi = x - ct$, with speed $c \in \mathbb{R}$, an a priori free $\mathcal{O}(1)$ parameter (w.r.t. the asymptotically small parameter ε). By setting

$$(B(x,t), W(x,t)) = (b(\xi), w(\xi)) \tag{1.5}$$

and introducing

$$p = b_\xi, \qquad q = \frac{1}{\varepsilon} w_\xi, \tag{1.6}$$

PDE (1.4) reduces to the four-dimensional 'spatial' dynamical system

$$\begin{cases} b_\xi &= p, \\ p_\xi &= wb^3 - wb^2 + (1-aw)b - cp, \\ w_\xi &= \varepsilon q, \\ q_\xi &= \varepsilon\left(-\Psi + \left[\Phi + \Omega b + \Theta b^2\right] w\right) - \varepsilon^2 cq. \end{cases} \tag{1.7}$$

The fully vegetated state and the bare soil state are equilibria of this system, while solutions connecting the two - so called heteroclinic orbits - represent interfaces of vegetation patterns and, hence, the fundamental entities to study in order to understand pattern formation.

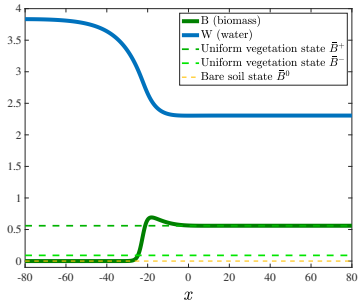

(a) Spatial profiles of the B- and W-components of a stationary front solution of the original, unscaled model (1.3) – corresponding to a stationary 1-front.

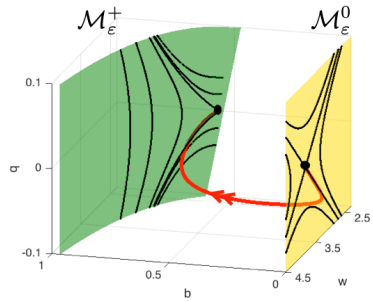

(b) The profile from **(a)** as a projection in (b, w, q)-space. The $B-$ and W-coordinates were extracted from the simulation of **(a)** and q was computed by numerical differentiation

Figure 1.4: (a) Profile of a stationary 1-front connection of the original, unscaled model (1.3) connecting the bare soil state to the vegetated state in real space **(a)** and in phase space **(b)**.

Although (1.7) represents a 4-dimensional system of ordinary differential equations (ODE's), it is still rather difficult to analyze in full. A "simple" connection between the bare soil state and the fully vegetated state as seen in the simulation from Figure 1.4a takes the complex geometrical form of Figure 1.4b when studied in the context of (1.7). The rigorous mathematical construction of such heteroclinic solutions in 4-D is a challenging task making use of various theories and techniques, the basics of which we review next.

2 Mathematical concepts

2.1 Reaction-diffusion equations, orbits and patterns

Similar to the complexity of ecosystems and ecology, only a limited amount of statements can be made about most nonlinear dynamical systems and their behavior [72]. Nonetheless, investigating their "somewhat" simpler parts, such as stationary or uniformly traveling solutions, yields a bigger understanding of the dynamics of the system than one might intend to think. In order to properly

address the questions that the dryland models in Chapter 2 and Chapter 3 present, some mathematical concepts and theorems are of indispensable importance.

The following can be seen as a stripped down, hands-on, guide to the basic understanding of the tools and techniques used in the following chapters, accompanied with a simple example to set the scene.

We are looking for stationary solutions of the reaction-diffusion equation

$$\frac{\partial u}{\partial t} = D\Delta u + f(u). \tag{1.8}$$

where $u(x,t) \in \mathbb{R}^m$ is a vector of state variables describing the densities of a population or a concentration at position $x \in \mathbb{R}^n \subset \Omega$ with Ω an open set, at time $t \subset \mathbb{R}^+$. On the right side of the equation, D represents a constant diagonal "diffusion" matrix, Δ represents the Laplacian operator working on u and $f(u)$ represents a smooth (nonlinear) vector field $f : \mathbb{R}^m \to \mathbb{R}^m$, the "reaction" term of the equation.

Introducing the traveling wave coordinate $\xi = x - ct$, with speed $c \in \mathbb{R}^n$, above solution is referred to as a traveling wave $\Phi(\xi) = \Phi(x - ct)$ if it satisfies

$$D\Phi'' + c\Phi' + f(\Phi) = 0. \tag{1.9}$$

Solutions to (1.9) can take different forms, from single fixed points to whole orbits/trajectories. This is quantified within the notion of invariant sets. An invariant set is a set such that a solution of (1.8) through each point of the set lies in the specific set for all time. We can further specify forward and backward invariant sets, respectively. A forward invariant set Λ^+ is a set for which $\Phi(\xi) \in \Lambda^+$ for all $\xi \geq \xi_+$. A backward invariant set Λ^- is a set for which $\Phi(\xi) \in \Lambda^-$ for all $\xi \leq \xi_-$. A rough sketch of invariant sets is given in Figure 1.5.

The notion of invariant sets can be cast in the more general notion of invariant manifolds. For sufficiently smooth systems, the invariant set represents an invariant manifold. For a detailed definition, we refer the reader to classical books on differential dynamical systems [104, 169]. Similar to forward and backward invariant sets, we can specify unstable and stable manifolds W^s and W^u for a set Λ, respectively:

$$W^s(\Lambda) = \{\xi_0 \in \mathbb{R}^n : \Phi(\xi, \xi_0) \to \Lambda \text{ for } \xi \to \infty\}, \tag{1.10}$$

$$W^u(\Lambda) = \{\xi_0 \in \mathbb{R}^n : \Phi(\xi, \xi_0) \to \Lambda \text{ for } \xi \to -\infty\}. \tag{1.11}$$

Again, for sufficiently smooth systems, $W^{s,u}(\Lambda)$ are differentiable manifolds.

Once we focus our attention on fixed points (equilibria) and trajectories connected to them, we can classify the different orbits (that are stationary in the

co-moving frame) we are interested in, depending on their behavior within the invariant sets:

- A **homoclinic orbit** $\gamma(p)$ is a closed orbit where the stable manifold $W^s(p)$ of a fixed point p intersects with the unstable manifold $W^u(p)$ of the same fixed point p, that is, $\gamma(p) \subset W^s(p) \cap W^u(p)$ and all points tend to the same fixed point p for $\xi \to \pm\infty$.
- A **heteroclinic orbit** A heteroclinic orbit $\gamma(p_1, p_2)$ is an orbit where for two different fixed points p_1 and p_2 the unstable manifold $W^u(p_1)$ of p_1 intersects with the stable manifold $W^s(p_2)$ of p_2, that is, $\gamma(p_1, p_2) \subset W^u(p_1) \cap W^s(p_2)$, and for which all points tend to p_1 and p_2 for $\xi \to -\infty$ and $\xi \to +\infty$, respectively.

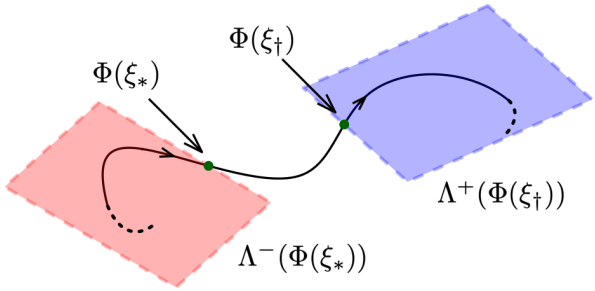

Figure 1.5: Sketch of unstable (blue) and stable (red) invariant sets Λ^+ and Λ^-, respectively, of a trajectory Φ. For every $\xi \geq \xi_\dagger$, it holds that $\Phi(\xi) \in \Lambda^+(\Phi(\xi_\dagger))$ and for every $\xi \leq \xi_*$, it holds that $\Phi(\xi) \in \Lambda^-(\Phi(\xi_*))$.

Besides these two orbits, frequently studied solutions are **periodic orbits**, to which Chapter 2 is basically dedicated. Periodic orbits have the characteristic that they contain no fixed points and that there exists a specific $0 < L < \infty$ with the property that $\Phi(\xi + L) = \Phi(\xi)$ for all $\xi \in \mathbb{R}^n$. This is equivalent to having a distinct wavenumber. A system of equations such as (1.8) generally displays a whole continuous families of periodic orbits [39]. From the point of view of the underlying PDE (1.8), these orbits are spatially periodic (traveling) 'wave trains'. Of course, one is especially interested in those wave trains that are stable and thus observable as solutions of the PDE. The family of stable "observable" periodic orbits within (parameter, wavenumber)-space is referred to as the "Busse balloon" [18]. This concept is extensively studied within Chapter 2, where theory and real world data are put side by side. A schematic representation of a section of a Busse balloon is given in Figure 1.6.

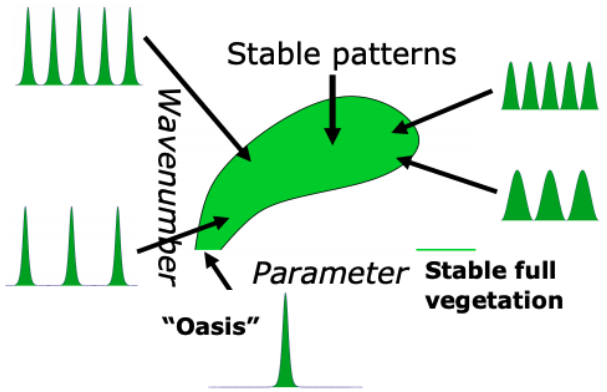

Figure 1.6: A schematic representation of a section of a Busse balloon, where the stable patterns are depicted in (parameter, wavenumber)-space. The green area encloses all stable periodic orbits. Outside this area the periodic patterns are unstable. As the parameter is declined, the patterns become narrower and vice versa. Per parameter value, there exists a whole set of observable stable patterns with different wavenumbers.

In order to get a visual understanding of the potential different patterns presented above, consider the following one-component toy model in one spatial dimension:

$$u_t = u_{xx} - u^3 - u^2 + (1-a)u \tag{1.12}$$

where $a \in \mathbb{R}$ is a free parameter we can vary. Note that this is the equivalent of PDE (1.8) in this simplified setting, with diffusion term $D\Delta u = u_x x$ and nonlinear reaction term $f(u) = u^3 - u^2 + (1-a)u$. Introducing $v = u_x$ and looking at stationary solutions, that is setting $u_t = 0$, we get the following two dimensional system of ODE's

$$\begin{cases} u_x &= v, \\ v_x &= u^3 - u^2 + (1-a)u, \end{cases} \tag{1.13}$$

System (1.13) represents a stripped down version of equation (1.9) where we have set for simplicity $c = 0$ (i.e., we only consider stationary patterns). It exhibits up to three fixed points, given by:

$$\begin{cases} (u_0, v_0) &= (0,0) \\ (u_\pm, v_0) &= \left(\dfrac{1 \pm \sqrt{4a-3}}{2}, 0 \right). \end{cases} \tag{1.14}$$

Clearly, for $a < \dfrac{3}{4}$, system (1.13) possesses only one fixed point $(u_0, v_0) = (0,0)$.

For $a = \frac{3}{4}$, it possesses two fixed points $(u_0, v_0) = (0, 0)$ and $(u_\pm, v_\pm) = (\frac{1}{2}, 0)$. For $a = 1$, it again possesses two fixed points $(u_0, v_0) = (u_-, v_0) = (0, 0)$ and $(u_+, v_0) = (1, 0)$. For $a \in (\frac{3}{4}, \infty)\backslash\{1\}$ we get three distinct fixed points as given in (1.14). Different values of a thus generate different possible connections - orbits - between the different fixed points. To illustrate the possible orbits we focus on the case where $a > \frac{3}{4}$. System (1.13) represents a Hamiltonian system. The solutions to the set of equations lay on the level sets of the Hamiltonian $\mathcal{H} = b$ with $b \in \mathbb{R}$ where

$$\mathcal{H}(u, v) = \frac{v^2}{2} - \frac{u^4}{4} + \frac{u^3}{3} - \frac{(1-a)u^2}{2}. \tag{1.15}$$

This yields *phase portraits*, that can look different, depending on the value of a, as can be seen in Figure 1.7.

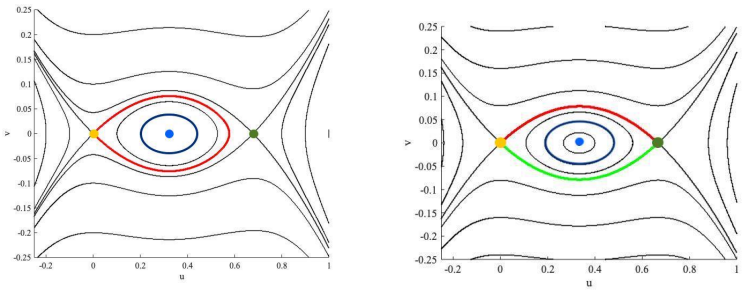

(a) Homoclinic orbit connecting the fixed point (u_0, v_0) to itself for $a = \frac{7}{9} + \frac{1}{250}$.

(b) Heteroclinic orbits connecting the fixed point (u_0, v_0) to the fixed point (u_+, v_0) with $a = \frac{7}{9}$. Note that due to the symmetry of the system we have two heteroclinic orbits (red and green).

Figure 1.7: Phase portraits of solutions of system (1.13).

Each orbit in a phase portrait corresponds to a distinct spatial pattern in real space associated to (1.13). A homoclinic orbit in the ODE (1.13) system corresponds to what is commonly referred to as a pulse in the PDE (1.12) as shown in Figure 1.8a, a heteroclinic orbit similarly corresponds to a 1-front connection (Figure 1.8b) and a periodic orbit simply corresponds to a periodic pattern (Figure 1.8c).

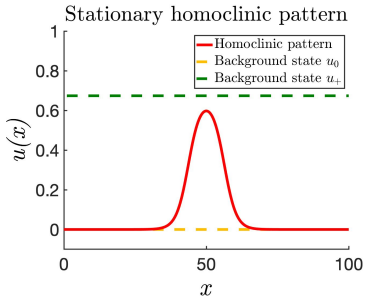

(a) The stationary homoclinic orbit corresponding to the phase portrait of Figure 1.7a and $a = \frac{7}{9} + \frac{1}{250}$.

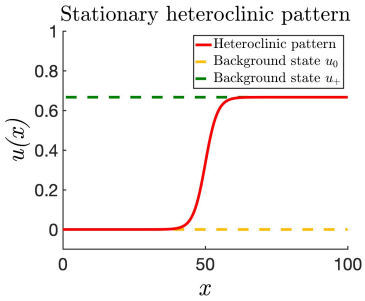

(b) The unique stationary heteroclinic orbit connecting (u_0, v_0) to (u_+, v_0) in the phase portrait of Figure 1.7b for $a = \frac{7}{9}$, where $v \geq 0 \ \ \forall x$.

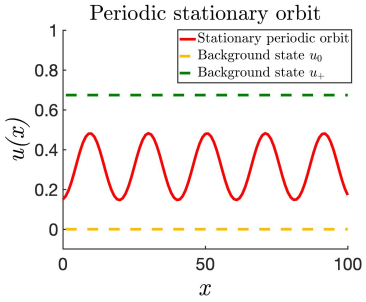

(c) A stationary periodic orbit for $a = \frac{7}{9} + \frac{1}{200}$.

Figure 1.8: Spatial profile of the different stationary patterns exhibited by system (1.12).

The analysis and spatial patterns extracted from toy model (1.12) are pretty simple and straightforward. The patterns obtained from toy model (1.12) are similar to those observed in real ecosystems, such as the ones described in Chapter 3, where the ecosystem model involved (1.3) is more realistic yet more mathematically involved. This yields the following "real ecosystem patterns counterpart" of the patterns in Figure 1.8.

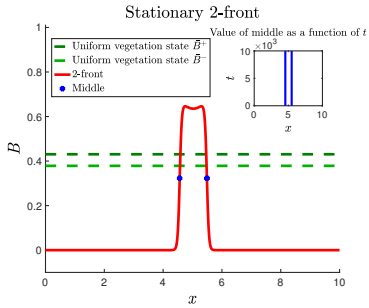

(a) A homoclinic stationary 2-front spot pattern of system (1.4).

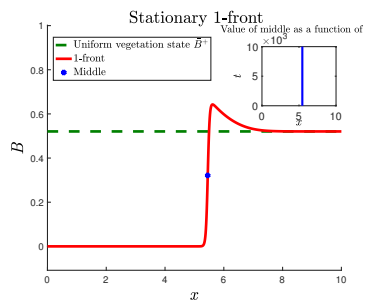

(b) The unique heteroclinic stationary 1-front pattern of system (1.4).

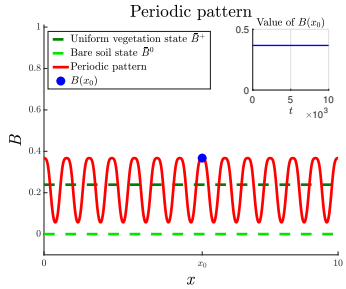

(c) A small amplitude stationary spatially periodic solution generated by a Turing bifurcation in system (1.4).

Figure 1.9: Spatial profile of the different patterns exhibited by system (1.4). For the exact parameter settings, we refer to section 4 of Chapter 3.

The spatial profile of the homoclinic and heteroclinic patterns of Figure 1.9 is non-monotonous, due to the geometry of the invariant slow manifolds of model (1.3). Due to the complexity of the model at hand, basic ODE solving tools often fail to deliver. Luckily, when it comes to connections, especially homoclinic and heteroclinic, a mathematical theory comes in handy: geometrical singular perturbation theory.

2.2 Geometric singular perturbation theory

Geometrical singular perturbation theory is a geometric approach revolving around scale separation within a dynamical system, as is the case in the models presented in Section 1.2. The geometric approach endeavors to identify the central dynamical structures such as invariant sets and invariant manifolds, present in the phase space of the system. Often within reaction-diffusion equations, the time evolution of different variables differs by several orders of magnitude. Similarly, their spatial evolution can take place on various length scales. A 'magnification' of (one of) these scale separations can be very insightful. Assumptions with respect to processes that have different time or length scales might simplify the problem we want to understand, yielding a first insight into the structures and dynamics involved. Assuming that very fast processes regulate instantly or that slow processes stand still are examples of these possible magnifications. They describe the system in some *limiting case*, which is usually easier to analyze mathematically. The foundation of this approach was set by Fenichel [51–54]. Since then, these mathematical methods have evolved and found their way towards applications, including ecological models. For a more mathematical introduction, including proofs of the theorems, we refer to the surveys of Jones [83] and Kaper [86].

Consider the system of singularly perturbed ordinary differential equations in general form:

$$\begin{cases} u_x = f(u, v, \varepsilon), \\ v_x = \varepsilon g(u, v, \varepsilon). \end{cases} \tag{1.16}$$

In the equation above, $u \in \mathbb{R}^m$, $v \in \mathbb{R}^n$. The constant real parameter ε is small, i.e., $0 < \varepsilon \ll 1$. The functions f and g are assumed to be sufficiently smooth. 'Sufficiently smooth' here means at least C^1 in u, v and ε.

A reformulation of system (1.16) in terms of the rescaled variable $y = \varepsilon x$ yields

$$\begin{cases} \varepsilon u_y = f(u, v, \varepsilon), \\ v_y = g(u, v, \varepsilon). \end{cases} \tag{1.17}$$

Systems (1.16) and (1.17) are equivalent for $\varepsilon \neq 0$. System (1.16) is referred to as the *fast system* and system (1.17) is referred to as the *slow system*. For $\varepsilon = 0$, the fast system (1.16) reduces to an m-dimensional *reduced fast system* on a manifold $\{f(u, v_0) = 0\}$ in $(m + n)$- dimensional space with the n-dimensional variable v as a constant parameter

$$\begin{cases} u_x = f(u, v_0, 0), \\ v = v_0. \end{cases} \tag{1.18}$$

For $\varepsilon = 0$, the slow system (1.17) reduces to an n-dimensional *reduced slow system* with

$$\begin{cases} 0 = f(u, v, 0), \\ v_y = g(u, v, 0). \end{cases} \tag{1.19}$$

Under (1.18) the solutions are defined in $\mathbb{R}^{m+n}$, but are in fact an n-parameter family of m-dimensional systems. Moreover, the solutions under (1.18) on the n-dimensional set $f(u, v, 0) = 0$ are trivial. On the other hand, (1.19) does prescribe a nontrivial solution on $f(u, v, 0) = 0$, but at the same time it is limited to only this set.

Geometric singular perturbation theory seeks to exploit the properties of these fast-slow decompositions and the intersections of various manifolds in order to establish the existence of different desired orbits (periodic, heteroclinic, homoclinic). The two reduced systems (1.18) and (1.19) offer different insights into the behavior of orbits and geometric structures in the fast and slow regimes, respectively, but in either formulation the $\varepsilon > 0$ system (1.16) can't be described in full. The goal of geometric singular perturbation theory is to analyze the dynamics of system (1.16) with ε nonzero but small by suitably combining the dynamics of the two limits of the reduced fast and slow systems. Certain geometric structures in the phase space of (1.16) with $0 < \varepsilon \ll 1$ can be found close to counterparts from (1.18). These structures are usually easier to locate. In addition, certain other geometric constructs of (1.16) with $0 < \varepsilon \ll 1$ lie close to objects in the phase space of (1.19). By exploiting this decomposition into fast and slow, the geometric approach reduces the full singularly perturbed system to separate lower-dimensional regular perturbation problems in the fast and slow regimes, respectively.

The basic ingredient is to combining these 'puzzle pieces' is illustrated in Figure 1.10 and is as follows. Suppose we are given an n-dimensional manifold $\mathcal{M}_0$ which is contained in the set $\{f(u, v, 0) = 0\}$. Note that this implies that $\mathcal{M}_0$ consists of critical points of the reduced fast system (1.18). Of all the systems like (1.16), we focus on the one for which the manifold $\mathcal{M}_0$ consists of only hyperbolic points of the reduced fast system (1.18), that is, critical points whose

eigenvalues λ of the Jacobian $\dfrac{\partial f}{\partial u}(u, v, 0)_{|\text{hyperbolic point}}$ are uniformly bounded away from the imaginary axis. Then the so-called critical manifold $\mathcal{M}_0$, is said to be normally hyperbolic, and persists as a *locally invariant slow manifold* $\mathcal{M}_\varepsilon$ of the full problem (1.16) that is $\mathcal{O}(\varepsilon)$ close to $\mathcal{M}_0$. The restriction of the flow (1.17) to $\mathcal{M}_\varepsilon$ is a small perturbation of the trajectories of the limiting problem (1.19). Moreover, the stable and unstable manifolds $\mathcal{W}^s(\mathcal{M}_0)$ and $\mathcal{W}^u(\mathcal{M}_0)$ of $\mathcal{M}_0$ persist as manifolds $\mathcal{W}^s(\mathcal{M}_\varepsilon)$ and $\mathcal{W}^u(\mathcal{M}_\varepsilon)$ too. They lie within $\mathcal{O}(\varepsilon)$ distance of, and are diffeomorphic to, $\mathcal{W}^s(\mathcal{M}_0)$ and $\mathcal{W}^u(\mathcal{M}_0)$ respectively [77]. These persistence theorems, proved by Fenichel [51–54], form the basis for the construction of global singular orbits. By 'gluing' together fast and slow pieces obtained in the fast and slow regimes, respectively, and verifying the persistence of these global structures for small $\varepsilon \neq 0$, the desired orbits can be obtained for the full system.

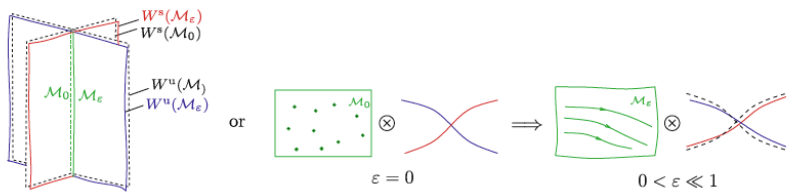

Figure 1.10: Unperturbed critical manifolds $\mathcal{M}_0$ consisting of fixed points ($\cdot$) and their local stable and unstable manifolds $W^{s,u}(\mathcal{M}_0)$. The manifolds persist for $0 < \varepsilon \ll 1$ as perturbed manifolds $\mathcal{M}_\varepsilon$ with trajectories on them [77].

3 The onset of patterns

The study of the formation and nonlinear evolution of ecosystems canonically emerges from combining the pre-requisites of Section 1 and Section 2 of this introduction. This section is focused on providing the mathematical mechanisms by which spatio-temporal heterogeneities may occur in a reaction-diffusion system, and their interpretation in terms of the underlying ecological mechanisms. In doing so, we lay out the basics of the localized structures considered in Chapter 2 and Chapter 3 of this thesis.

Consider equation (1.8), in the simplest case that still generates rich pattern dynamics, that is, a 2-component reaction-diffusion equation in one spatial dimension, the unbounded domain $\mathbb{R}$:

$$\begin{cases} u_t = u_{xx} + f(u, v; \mu), \\ v_t = dv_{xx} + g(u, v; \mu), \end{cases} \tag{1.20}$$

where $u(x, t), v(x, t) \in \mathbb{R}$ with $x \in \mathbb{R}$ and $t \in \mathbb{R}^+$. The coefficient d is a constant diffusion coefficient and the vector fields $f(u, v; \mu), g(u, v; \mu) : \mathbb{R}^2 \to \mathbb{R}^2$ represent the reaction terms of the equations where we specified their dependence on (a number of) constant parameters $\mu \in \mathbb{R}^m$ of the system.

In the ecological setting of this thesis, system (1.20) models the spatial interactions between biomass density and water in vegetation ecosystems on a flat terrain. In reality, ecosystems are subject to another spatial property of their environment: its topography. This is characterized by the (local) slope of the terrain, which can have a significant effect on the vegetation dynamics. It has been observed that vegetation aligns in resilient striped patterns perpendicular to the slope of the terrain due to an oriented flow of water downhill [6, 9, 33, 101, 152]. Therefore, we will study the effect of the presence of slope on the classical 'flat terrain' Turing destabilization.

Including slope into system (1.20), the displacement of water is mathematically modeled as a combined effect of diffusion (dv_{xx}) and advection (sv_x), where $s \in \mathbb{R}$ is a measure for the slope of the terrain [90]. The latter is a topographical effect, which in general depends on the spatial variable x, that is, takes the form $h(x)$. This would yield addition terms $h_x v_x + h_{xx} v$ in (1.20) [11].Thus by modeling the topographical effect as sv_x with s a constant, we consider the case of a constant slope, $h(x) \equiv sx$.

In the general mathematical setting of the system (1.20), we thus extend the reaction-diffusion equation into a (2-component) reaction-advection-diffusion

equation (in one spatial dimension) of the form

$$\begin{cases} u_t = u_{xx} + f(u, v; \mu), \\ v_t = dv_{xx} + sv_x + g(u, v; \mu). \end{cases} \tag{1.21}$$

In the ecological setting, v represents the water equation, where the diffusion coefficient $d \gg 1$ as water diffuses on a much faster timescale than vegetation disperses, the latter being described by the u-equation. Since $v_t = sv_x$ yields $v = v(x + st)$, i.e., an advective transport with speed $-s$, this means that increasing x corresponds to the uphill direction. Moreover, for the case $s = 0$, system (1.21) is equivalent to system (1.20), which has been studied extensively in [39] and the references therein.

Denote the trivial background states of (1.20) and (1.21) as (U, V), for which we know that $f(U, V) = g(U, V) = 0$. Note that the stationary solutions are the same for both systems, as the additions of the sv_x term does not alter the steady state solutions.

The spectral – or linearized – stability of (U, V) of system (1.21) against (bounded) perturbations can be determined by plugging the decomposition,

$$\begin{pmatrix} u(x,t) \\ v(x,t) \end{pmatrix} = \begin{pmatrix} U \\ V \end{pmatrix} + \begin{pmatrix} u_p \\ v_p \end{pmatrix} \tag{1.22}$$

with

$$\begin{pmatrix} u_p \\ v_p \end{pmatrix} = \begin{pmatrix} \alpha \\ \beta \end{pmatrix} e^{ikx+\lambda t} + c.c. \tag{1.23}$$

into (1.21), with $k \in \mathbb{R}$, $\lambda \in \mathbb{C}$ and $(\alpha, \beta) \in \mathbb{C}^2$. The linearized 2×2 eigenvalue problem is then determined by

$$\mathcal{A}(k; \mu) \begin{pmatrix} \alpha \\ \beta \end{pmatrix} = \begin{pmatrix} f_u - k^2 & f_v \\ g_u & g_v - dk^2 + isk \end{pmatrix} \begin{pmatrix} \alpha \\ \beta \end{pmatrix} = \lambda \begin{pmatrix} \alpha \\ \beta \end{pmatrix} \tag{1.24}$$

with

$$f_u = \frac{\partial f}{\partial u}(U(\mu), V(\mu); \mu), f_v(\mu) = \frac{\partial f}{\partial v}(U(\mu), V(\mu); \mu), \text{etc.} \tag{1.25}$$

Since $k \in \mathbb{R}$, the associated characteristic polynomial,

$$\lambda^2 - \lambda[(f_u + g_v - (1+d)k^2 + isk] + [dk^4 - (g_v + df_u)k^2 + (f_u g_v - g_u f_v)] + isk(f_u - k^2) = 0 \tag{1.26}$$

defines 2 functions $\lambda_{1,2} : \mathbb{R} \to \mathbb{C}$ which we assume to be ordered; $\mathrm{Re}(\lambda_2(k)) \leq \mathrm{Re}(\lambda_1(k))$. Note that λ_j is symmetric in k for $s = 0$ while $\lambda(-k) = \bar{\lambda}(-k)$ for

$s \neq 0$.

A trivial background state (U, V) of (1.21) is spectrally stable for those values of the parameter μ for which $\mathrm{Re}(\lambda_{1,2}(k;\mu)) < 0$ for all $k \in \mathbb{R}$. Pattern formation sets in (from (U, V)) as μ crosses through a critical value μ_c beyond which there are values of k for which $\mathrm{Re}(\lambda_1(k;\mu)) > 0$. Here we focus on the Turing mechanism , i.e., we assume that (U, V) is marginally stable at $\mu = \mu_c$ and that there is a $k_c \neq 0$ such that $\mathrm{Re}(\lambda_1(\pm k_c;\mu_c)) = 0$ while $\mathrm{Re}(\lambda_1(k;\mu_c)) < 0$ for all $k \in \mathbb{R}$ with $k \neq \pm k_c$. Note that this implicitly implies that $\mathrm{Re}(\lambda_{1,2})(0,\mu_c) < 0$, i.e., that (U, V) is stable against spatially homogeneous perturbations [113, 150]. It follows from the smoothness of $\lambda_{1,2}(k;\mu)$, that $k = k_c$ must be a local maximum of $\mathrm{Re}(\lambda_1(k;\mu_c)) : \mathrm{Re}(\frac{d\lambda_1}{dk}(\pm k_c;\mu_c)) = 0$ for all k in neighborhoods of $\pm k_c$.
Analyzing this for the classical case $s = 0$ yields

$$k_c = k_c(\mu) = \pm\sqrt{\frac{df_u + g_v}{2d}} \quad \text{with} \quad df_u + g_v > 0., \tag{1.27}$$

(see for instance [39, 113]). The critical value μ_c can be computed by plugging (1.27) back into (1.26). Further manipulations, for which we refer the reader to [39], yield the classical conditions for the destabilization by the Turing mechanism

$$f_u > 0, g_v < 0, \tag{1.28}$$
$$f_u + g_v < 0, \tag{1.29}$$
$$f_u g_v - f_v g_u > 0, \tag{1.30}$$

where we have used that $d > 1$. Note that the two components $u(x,t)$ and $v(x,t)$ are thus diffusing with different speeds, thereby fulfilling the roles of an *activator u* and an *inhibitor v* within the equation, that is, $f_u(U(\mu_c), V(\mu_c);\mu_c) > 0$ and $g_v(U(\mu_c), V(\mu_c);\mu_c) < 0$ Figure 1.11, depicts two different critical eigenvalue curves $\lambda_{1,2}(k)$ for the distinct possible cases in the classical scenario $s = 0$.

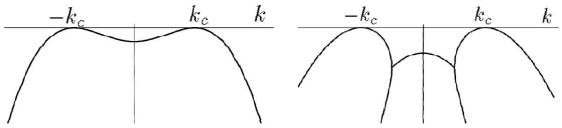

Figure 1.11: Two critical eigenvalue curves in the classical case $s = 0$. (a,b): The real parts of the solutions $\lambda_{1,2}(k)$ of (1.26) for a Turing destabilization, i.e., $k_c \neq 0$ with $\lambda_{1,2}(k) \in \mathbb{R}$ for all $k \in \mathbb{R}$ in (a), and parameter combinations such that $\lambda_{1,2}(k) \notin \mathbb{R}$ for certain k in (b) citeDreview.

To investigate the impact of the slope on the classical Turing bifurcation and to minimize the technicalities of the stability analysis, we assume that s is small, i.e., we introduce $0 < \delta \ll 1$ and set $s = \delta\tilde{s}$.

We know from the above classical Turing analysis that $\lambda_1(k;\mu)$, that is, the critical λ_j, is real for (k,μ) close to (k_c,μ_c). Thus we may conclude from (1.26) that

$$\lambda_1(k;\mu) = \lambda_r(k;\mu) + \lambda_i(k;\mu) = \lambda_r + i\delta\tilde{\lambda}_i(k;\mu) \tag{1.31}$$

A straightforward perturbation analysis yields that

$$k_c(s) = k_c(0) + \mathcal{O}(\delta^2) \quad \text{and} \quad \mu_c = \mu_c(0) + \mathcal{O}(\delta^2), \tag{1.32}$$

with $k_c(0), \mu_c(0)$ as determined by the classical Turing analysis (i.e., in (1.20)/(1.21) with $s = 0$ – see Appendix 1.A). That same analysis yields

$$\lambda_i(k_c) = \delta\tilde{\lambda}_i(k_c) = -\frac{\tilde{s}}{d-1}k_c\delta + \mathcal{O}(\delta^3). \tag{1.33}$$

Thus we find by (1.22) that the most critical perturbation, i.e., the perturbation that is the first to start growing at the Turing destabilization is given by

$$\begin{pmatrix} u_p \\ v_p \end{pmatrix} \sim \begin{pmatrix} \alpha_c \\ \beta_c \end{pmatrix} e^{ik_c x + \lambda(k_c,\mu_c)t} + c.c. = \begin{pmatrix} \alpha_c \\ \beta_c \end{pmatrix} e^{ik_c\left(x - \frac{\delta\tilde{s}}{d-1}t\right)(1+\mathcal{O}(\delta^2))} + c.c. \tag{1.34}$$

and travels with speed

$$c = \frac{\delta\tilde{s}}{d-1} + \mathcal{O}(\delta^3). \tag{1.35}$$

The interpretation in terms of (1.21) as ecosystem model in biomass u and water v confirms the ecological intuition that vegetation patterns should move uphill: as was already argued, the term sv_x in (1.21) determines the downhill direction by its associated 'advective speed' $= -s$. Since water diffuses much faster than biomass, i.e., $d \gg 1$, in (1.35) Turing patterns travel in the opposite direction: biomass travels towards the down flowing water.

While the conditions for the onset of a Turing destabilization are relatively straightforward, the determination of the nature of the pattern that is exhibited is a more difficult problem since beyond the bifurcation point, a finite band of wavenumbers is growing exponentially. Therefore, it is *a priori* unclear whether the perturbations also evolve into stable (spatially periodic) Turing patterns. This is actually only the case if the associated Turing bifurcation is supercritical [39]. The nature of the Turing bifurcation can be determined by a weakly nonlinear amplitude equation approach – we refrain from going in the details here.

4 Content of thesis

The nature of the research done in this thesis is diverse. Two different "paths" have been taken in executing interdisciplinary research in ecology and mathematics through the lens of pattern formation as will become clear in Chapter 2 and Chapter 3. Nonetheless, the foundation of the work at hand is concordant: an ecological phenomenon is modeled with explicit two-component ecosystem models, allowing for rigorous mathematical analysis and numerical computations, that reproduce the patterns observed in nature. The mixture of analyzing the underlying mathematical structure of the ecosystem model and exploring the ecological data and parameters at hand allows for a deeper understanding of the mechanisms at play, thereby leading to qualitative conclusions about the ecosystem, the patterns it exhibits and the knowledge thereof. This represents a step towards a better comprehension and theoretical predictions of the behavior of the process of desertification as well as pattern formation in ecosystems. The work done in this thesis even goes beyond the latter, by unraveling new insights in both the ecological and mathematical community.

4.1 Multistability of striped vegetation patterns

Chapter 2, titled "*Multistability of model and real dryland ecosystems through spatial self-organization*"[1], represents a novel study providing a meticulous comparison between theoretical model predictions and empirical data of spatial vegetation patterns in dryland ecosystems.

Model predictions by the extended-Klausmeier model, which exhibits different patterns (such as bands and gaps) are put side by side with state of the art aerial and topographical observations of banded vegetation patterns obtained in two regions in Somalia and characteristics thereof (biomass density, spatial spread of bands). Since it is considered the most "conceptual" reaction-diffusion model at hand for these types of ecosystems, the extended-Klausmeier model constitutes a perfect candidate to assess basic yet fundamental correlations between theory and data.

Regularly spaced banded vegetation patterns have long been considered to be leading indicators for the proximity of an ecosystem to desertification and changes thereof. They are characterized by their wavenumber/period as well as their size and biomass density. In this study, we establish multi-stability of banded vegetation patterns, which implies the co-existence of a whole (continu-

[1] Joint work with Robbin Bastiaansen, Vincent Deblauwe, Maarten B. Eppinga, Koen Siteur, Stéphane Mermoz, Alexande Bouvet, Arjen Doelman and Max Rietkerk; has appeared as publication in *PNAS* [13].

ous) range of wavenumbers of significant spread, for the same set of parameters of the ecosystem model. That is, an ecosystem can display a whole family of stable (i.e., observable) banded patterns for a given set of parameters. This is theoretically contained in the notion of Busse balloon, the set of stable spatially-periodic solutions in (parameter, wavenumber)-space to the reaction-diffusion model. The concept of Busse balloon introduces the possibility of an ecosystem to increase its resilience - a mechanism that cannot take place in the classical mono-stable point of view and which thus offers a way to avoid collapse into the desert state. A disruption of stable banded patterns in a relatively large region was thought to result in a catastrophic shift towards desertification, with the disappearance of all vegetation bands. This study indicates that once a stable banded pattern is destabilized due to environmental changes, it may adapt its wavenumber (as well as its biomass density) to a new value which might still be contained within the Busse balloon, therefore still being stable (thus observable), making the shift in ecosystem change less drastic.

For this study, we did not consider changes in yearly rainfall, as the data over longer time periods was insufficient. Therefore, the main parameter worked with in the Busse balloon was the local slope of the terrain, using topographical and biomass data to gather precise information about the two regions studied.
In addition to the notion of multi-stability, this study shows a vast spread in the wavenumber, biomass density and migration speed of banded vegetation patterns of the site, further corroborating model predictions thereof.

4.2 Existence of (novel) localized vegetation patterns in a generalized ecosystem model

Chapter 3, titled "*The existence of localized vegetation patterns in a systematically reduced model for dryland vegetation*"[2], focuses on the two-component reaction-diffusion model for vegetation biomass and soil water content, as introduced in (1.3), which was obtained in Appendix 3.B by a systematic reduction of the three-component Gilad et al. model for dryland ecosystem dynamics [62]. The starting motivation was to gain a fundamental understanding of the underlying mathematical mechanism behind the infamous 'fairy circles' of the Namibian Desert presented in [175], which are localized extended gaps patterns (with an excess of vegetation at the edge). For this, the local two-component model obtained in Appendix3.A is fully adequate, given the environmental characteristics of the present vegetation and soil (such as confined root systems and sandy soil). Exploring the model in this context resulted in a change of course and a broadening of the study. The goal of this study then became two-fold: first, to analytically prove the existence of a multitude of vegetation patterns that have

[2]Joint work Arjen Doelman, Martina Chirilus-Bruckner and Ehud Meron; has appeared as publication in *Physica D* [82].

been observed in nature and can be found in numerical simulations of the model [175]. Second, to go beyond the existing observations and exploit the nonlinear richness of the model at hand in order to successfully construct and prove the existence of novel, both from an ecological and mathematical perspective, multi-front patterns.

In comparison to more conceptual models, such as the much studied extended-Klausmeier model, the Gilad et al. model possesses a more involved nonlinear structure. Although this yields a more complicated mathematical analysis, it has a strong advantage in that it can be more directly linked to ecological mechanisms and observations. That being said, no basic mathematical analysis on the patterns generated by the Gilad et al. model had been done before, until this study. Therefore, an in depth analysis and set-up of the basic mathematical characteristics of the model is required. This has been done in detail in the first part of the study, where the slow/fast dynamics of the 4-dimensional spatial ODE as presented in (1.7) are analyzed.

Building on this, a geometric singular perturbation analysis is applied to the rescaled version of the model introduced in (1.3). Geometric singular perturbation theory addresses the disparate length scales associated with biomass and water, and focuses on the strongly nonlinear 'far-from-equilibrium' regime, where desertification transitions typically take place and vegetation patterns exist.

The study proves the existence of 'basic' 1-front invasion patterns and 2-front spot/gap patterns which have a direct ecological interpretation and appear to be stable in simulations of the model. In fact, the existence of novel countably many distinct traveling 1-front patterns connecting the bare soil to the vegetated state is established as well as the existence of (traveling) 2-front spot and gap patterns for a whole open set of parameters of the model. A glimpse of the various patterns simulated and constructed can be seen in Figure 1.12.

The basic 1- and 2-front patterns, in addition, form the building blocks of the novel multi-front patterns. Based on the fast/slow dynamics of the 4-dimensional ODE, a whole set of localized vegetation spots embedded in bare soil with a varying number of spatial oscillations is constructed, as well as periodic versions of the latter as presented in Figure 1.12. In fact, we argue that these orbits/patterns are not specific for the model considered here, but will also occur in a much more general (singularly perturbed reaction-diffusion) setting as well as in an ecological setting. The study calls for further analysis of the findings in terms of (spectral) stability of the constructed (multi-)front patterns and their application in terms of ecology.

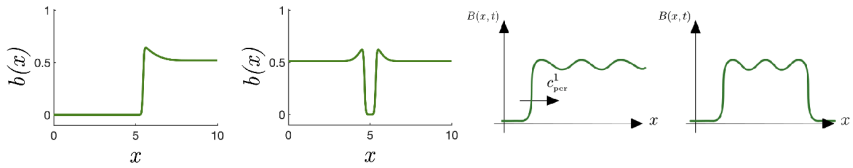

Figure 1.12: *Left half :* Two basic patterns exhibited by numerical simulations of model (1.3): a traveling (heteroclinic) invasion front and a stationary homoclinic, 2-front vegetation gap, i.e., a fairy circle. *Right half:* Two sketches of 'higher order' localized patterns constructed in Chapter 3: a 1-front connection between the bare soil state and a spatially periodic vegetation state and a representation of a 'higher order' localized (stationary, homoclinic 2-front) spot pattern with a countable number of 'spatial oscillations'.

Appendices

1.A Turing bifurcation on sloped terrains

By setting

$$s = \delta\tilde{s}, \qquad \lambda = \lambda_r + i\lambda_i = \lambda_r + i\delta\tilde{\lambda}_i, \quad 0 < \delta \ll 1 \tag{1.A.36}$$

equation (1.26) expands to

$$\begin{aligned} \lambda_r^2 \quad &+ \quad 2i\delta\lambda_r\tilde{\lambda}_i + \delta^2\tilde{\lambda}_i^2 - \lambda_r[(f_u + g_v) - (1+d)k^2] \\ &- \quad i\delta\tilde{\lambda}_i[(f_u + g_v) - (1+d)k^2] \qquad - i\lambda_r\tilde{s}\delta k + \tilde{\lambda}_i\tilde{s}\delta^2 k \\ &+ \quad [dk^4 - (g_v + df_u)k^2 + (f_u g_v - g_u f_v)] + i\delta\tilde{s}k(f_u - k^2) = 0. \end{aligned} \tag{1.A.37}$$

Isolating both real and complex parts of (1.A.37) gives:

Re:

$$\lambda_r^2 + \delta^2\tilde{\lambda}_i^2 - \lambda_r[(f_u+g_v) - (1+d)k^2] + \tilde{\lambda}_i\tilde{s}\delta^2 k + [dk^4 - (g_v+df_u)k^2 + (f_u g_v - g_u f_v)] = 0. \tag{1.A.38}$$

Im:

$$2\delta\lambda_r\tilde{\lambda}_i - \delta\tilde{\lambda}_i[(f_u + g_v) - (1+d)k^2] - \lambda_r\tilde{s}\delta k + \delta\tilde{s}k(f_u - k^2) = 0. \tag{1.A.39}$$

At $k = k_c$: it holds that $\dfrac{\partial\lambda_r}{\partial k} = \lambda_r = 0$. This gives

$$\begin{cases} 4dk^3 - 2(g_v + df_u)k + \delta^2(-2\tilde{\lambda}_i\tilde{\lambda}_{i,k} + \tilde{s}\tilde{\lambda}_i + \tilde{s}k\tilde{\lambda}_{i,k}) = 0, \\ -\tilde{\lambda}_{i,k}[(f_u + g_v) - (1+d)k^2] + 2\tilde{\lambda}_i(1+d)k + \tilde{s}(f_u - 3k^2) = 0. \end{cases} \tag{1.A.40}$$

At $\lambda_r = 0$ we get

$$\begin{cases} dk^4 - (g_v + df_u)k^2 + (f_u g_v - g_u f_v) + \delta^2\tilde{\lambda}_i(\tilde{s}k - \tilde{\lambda}_i) = 0, \\ -\tilde{\lambda}_i[(f_u + g_v) - (1+d)k^2] + \tilde{s}k(f_u - k^2) = 0. \end{cases} \tag{1.A.41}$$

Expanding k_c as

$$k_c = k_{c,0} + \delta^2 k_{c,2} + \dots \tag{1.A.42}$$

yields

$$4dk_{c,0}^3 - 2(g_v + df_u)k_{c,0} = 0. \tag{1.A.43}$$

which confirms that here that kc_0 is the critical wave number of the standard Turing bifurcation (i.e., for $s = 0$). Substituting this in equation (1.A.41) for $\tilde{\lambda}_i$ yields:

$$-\tilde{\lambda}_i[(f_u + g_v) - (1 + d)k_{c,0}^2] + \tilde{s}k_{c,0}(f_u - k_{c,0}^2) = \mathcal{O}(\delta^2) \tag{1.A.44}$$

and thus

$$\begin{aligned}
\tilde{\lambda}_i(k_c) &= \frac{f_u - k_{c,0}^2}{(f_u + g_v) - (1 + d)k_{c,0}^2} \cdot \tilde{s}k_{c,0} + \mathcal{O}(\delta^2) && \text{(1.A.45)}\\
&= \frac{f_u - \dfrac{g_v + df_u}{2d}}{(f_u + g_v) - (1 + d)\dfrac{g_v + df_u}{2d}} \cdot \tilde{s}\sqrt{\frac{(g_v + df_u)}{2d}} + \mathcal{O}(\delta^2) && \text{(1.A.46)}\\
&= -\frac{\tilde{s}}{d - 1} \cdot k_c + \mathcal{O}(\delta^2). && \text{(1.A.47)}
\end{aligned}$$

This confirms (1.32) and (1.33),

$$\lambda_i(k_c) = -\frac{\delta\tilde{s}}{d - 1} \cdot k_c + \mathcal{O}(\delta^3), \quad \mu_c = \mu_{c,0} + \mathcal{O}(\delta^2). \tag{1.A.48}$$